

Seismic Data Interpolation based on Denoising Diffusion Implicit Models with Resampling

Xiaoli Wei, Chunxia Zhang, *Member, IEEE*, Hongtao Wang, Chengli Tan, Deng Xiong, Baisong Jiang, Jiangshe Zhang, Sang-Woon Kim, *Life Senior Member, IEEE*

Abstract—The incompleteness of the seismic data caused by missing traces along the spatial extension is a common issue in seismic acquisition due to the existence of obstacles and economic constraints, which severely impairs the imaging quality of subsurface geological structures. Recently, deep learning-based seismic interpolation methods have attained promising progress, while achieving stable training of generative adversarial networks is not easy, and performance degradation is usually notable if the missing patterns in the testing and training do not match. In this paper, we propose a novel seismic denoising diffusion implicit model with resampling. The model training is established on the denoising diffusion probabilistic model, where U-Net is equipped with the multi-head self-attention to match the noise in each step. The cosine noise schedule, serving as the global noise configuration, promotes the high utilization of known trace information by accelerating the passage of the excessive noise stages. The model inference utilizes the denoising diffusion implicit model, conditioning on the known traces, to enable high-quality interpolation with fewer diffusion steps. To enhance the coherency between the known traces and the missing traces within each reverse step, the inference process integrates a resampling strategy to achieve an information recap on the former interpolated traces. Extensive experiments conducted on synthetic and field seismic data validate the superiority of our model and its robustness to various missing patterns. In addition, uncertainty quantification and ablation studies are also investigated.

Index Terms—Seismic data interpolation, denoising diffusion model, multi-head self-attention, resampling

I. INTRODUCTION

SEISMIC exploration interprets geological information and infers subsurface properties by analyzing the pre-stack data collected by geophones planted in the field. Acquisition of high-quality seismic data is a key factor for high-quality seismic data processing and interpretation. However, the collected seismic data is usually severely degraded due to the complex natural environment or limited budget. The degradation of data integrity is typically observed in the form of random or

consecutive missing seismic traces, resulting in undersampled or aliased seismic data [1].

Seismic data interpolation has been extensively investigated over the past decades. Initially developed traditional methods often rely on the assumption of global or local linear events to convert the problem into an autoregressive framework [2]. Especially, prediction-filter-based methods, combined with the t - x and f - x regularization [3], [4], occupy the research mainstream in this direction. Besides, wave-equation-based methods are able to extrapolate and interpolate wave field [5], whereas they require additional information, e.g., wave velocity. Two successful categories of model-driven methods involve different constraints to recover seismic data. The first category is the sparsity-based method, which introduces various sparse transforms and sampling functions to interpolate missing data [6–8]. Among these methods, those derived from the projection onto convex sets [9–11] have received more attention due to their relatively high performance. The second category applies the low-rank constraint model to recover data, e.g., using singular value decomposition on block Hankel matrix [12–14]. While the traditional methods and model-driven methods are capable of achieving interpolation from a theoretical perspective, issues such as manual parameter selection and enormous computation cost cannot be ignored, particularly for massive and high-dimensional field seismic data with advancements in collection technology and efficiency.

With the rapid advancement of deep learning-based generative models, the research focus for seismic data interpolation has shifted towards data-driven methods, which mainly include two categories, i.e., generative neural network and generative adversarial network (GAN). The preliminary methods in the first category of data-driven models contain the convolutional autoencoder (CAE) [15], [16], U-Net [17], [18], and residual network (ResNets) [19], etc. Liu *et al.* [20] introduce the invertible discrete wavelet transform for replacing the pooling operations in the traditional U-Net model, thereby avoiding the loss of detailed features caused by the downsampling scheme. Some researchers have worked on improving the long-range feature correlation via different attention modules [21], [22], which are critical to maintain the global content consistency, especially under the circumstance of consecutively missing seismic traces [23]. Furthermore, regularization terms are important in finding the optimal interpolation function, e.g., spectrum suppression [24] and regeneration constraint [25]. Some studies also focus on improving the seismic feature extraction ability of neural networks, including the adoption of UNet++

Corresponding author: Chunxia Zhang. E-mail: cxzhang@mail.xjtu.edu.cn. Xiaoli Wei, Chunxia Zhang, Hongtao Wang, Chengli Tan, Baisong Jiang, Jiangshe Zhang are with the School of Mathematics and Statistics, Xi'an Jiaotong University, Xi'an, Shaanxi, 710049, China.

Deng Xiong is with the Geophysical Technology Research and Development Center, BGP, Zhuozhou, Hebei, 072751, China

Sang-Woon Kim is with the Department of Computer Engineering, Myongji University, Yongin, 17058, South Korea.

This research was supported by the National Key Research and Development Program of China (No. 2018AAA0102201) and the National Natural Science Foundation of China (No. 61976174).

This work has been submitted to the IEEE TGRS for possible publication. Copyright may be transferred without notice, after which this version may no longer be accessible.

with a nested architecture [26] and dynamically updating the valid convolution region [27]. However, a standalone neural network is usually insufficient to capture the vast range of dynamic energy in seismic data. To resolve this issue, the coarse-refine network [28] and the multi-stage active learning method [29] have been proposed, which exploit the strengths of every sub-network to make the interpolation process more efficient and well-performed. The second category of data-driven models, GAN-based methods, has achieved impressive results in seismic data interpolation. Kaur *et al.* [30] adopt the framework of CycleGAN to perform self-learning on the seismic features. The conditional generative adversarial network (CGAN) is introduced to interpolate the seismic data with consecutively missing traces [31]. Based on CGAN, the dual-branch interpolation method combining the time and frequency domains improves the smoothness and quality of the reconstructed seismic data [32]. The large obstacle is a common trouble in seismic exploration, which leads to big gaps in the collected seismic data and impairs the further data processing. The promising results of conditional Wasserstein generative adversarial networks with gradient penalty (WGAN-GP) have revealed the seismic feature generation capability [33], whose gradient penalty enhances the fidelity of reconstructed signals at large intervals by enforcing the Lipschitz constraint. The coarse-to-fine learning strategy driven by the joint of different loss strengthens the connection between different stages and enables relativistic average least-square generative adversarial network (RaLSGAN) to produce more accurate and realistic signal details [34].

Although the deep learning-based seismic data interpolation method has attracted considerable attention, the instability of GAN training and the complexity of field data still limit its further development. First, while the generator can be implemented with a state-of-the-art generative architecture toward seismic data reconstruction, the demand for training the discriminator cannot be avoided for a GAN-based model, and the optimal solution often lies in a saddle point instead of a local minimum [35]. Stable adversarial training requires good initialization and hyperparameter settings. Second, field seismic data usually consist of multiple missing forms due to the influence of ground obstacles and geophone layout conditions, etc. The aforementioned data-driven methods either serve to a specific missing form of seismic data or need retraining when interpolating seismic data with different missing ratios or forms. Since their training is based on a certain mask distribution, the performance of the model may degrade to varying degrees or even fail to achieve the desired effect when transferring to a new scenario.

In this paper, we propose a new seismic denoising diffusion implicit model with resampling (SeisDDIMR) to address the above issues, showing that it only needs to be trained once to complete the reconstruction tasks of different missing rates or missing forms, and it exhibits superior interpolation effects compared to the existing deep learning methods. This denoising diffusion model-based approach retains the strong power of generative neural networks since the backbone can be inherited from state-of-the-art generative architectures. The main contributions of this paper are summarized below:

- Our model's entire training framework is built on denoising diffusion probabilistic models (DDPM) [36], which include two parameterized Markov chains, i.e., a forward diffusion process and a reverse process. The forward diffusion process progressively adds pre-designed Gaussian noise to the initial full seismic data. The reverse process uses variational inference to estimate the noise after a finite time of the forward process under the fixed noise addition mode, and thereby the parameterization estimation of the neural network is completed.
- Our noise matching network follows the U-Net structure equipped with multi-head self-attention (MHSA), which can capture stronger long-range correlations of seismic data.
- The inference process of our model deriving from condition interpolation is accelerated by using denoising diffusion implicit models (DDIM) [37], and we adopt the strategy of resample iterations [38] to enhance the consistency of the interpolation content before and after the reverse diffusion step. To make more effective adjustments conditioned on the known seismic traces, we introduce a cosine noise schedule that enables the inverse process to generate meaningful reconstruction signals in the early stages instead of high-noise results under a linear noise schedule. This contributes greatly to the interpolation quality.
- Existing deep learning methods are often limited by the missing forms constructed during training, consequently lacking robustness to effectively interpolate seismic data in cases where the missing patterns do not match or complex missing forms coexist. Our proposed method breaks through this issue and brings greater flexibility to the application of deep learning interpolation methods in field scenarios.

The remainder of this paper is organized as follows. In Section II, we introduce our SeisDDIMR method including the training, inference, and network architecture. In Section III, experiments with various missing interpolation are performed for both synthetic and field seismic data. The effectiveness of our method is demonstrated by comparing it with popular methods. Furthermore, to indicate the stronger advantages of our model in practical application scenarios, we conduct uncertainty quantification and model robustness validation. Section IV presents some ablation studies. Finally, we make conclusions and discussions in Section V.

II. METHODOLOGY

Let $\mathbf{x} \in \mathcal{R}^{n_r \times n_t}$ as the original complete seismic data, with n_r and n_t as the number of traces and time samples. The degradation process of observed seismic data can be formally expressed as

$$\mathbf{y} = \mathbf{m} \odot \mathbf{x}, \quad \text{such that} \quad \mathbf{m}[i, :] = \begin{cases} \mathbf{J}, & i \text{ is valid} \\ \mathbf{0}, & \text{else} \end{cases}$$

where \odot represents the element-wise multiplication, \mathbf{J} is the all-ones matrix, and $\mathbf{0}$ denotes the zero matrix. The notation $\mathbf{m}[i, :]$ indicates the missing mask of i th trace data. Seismic

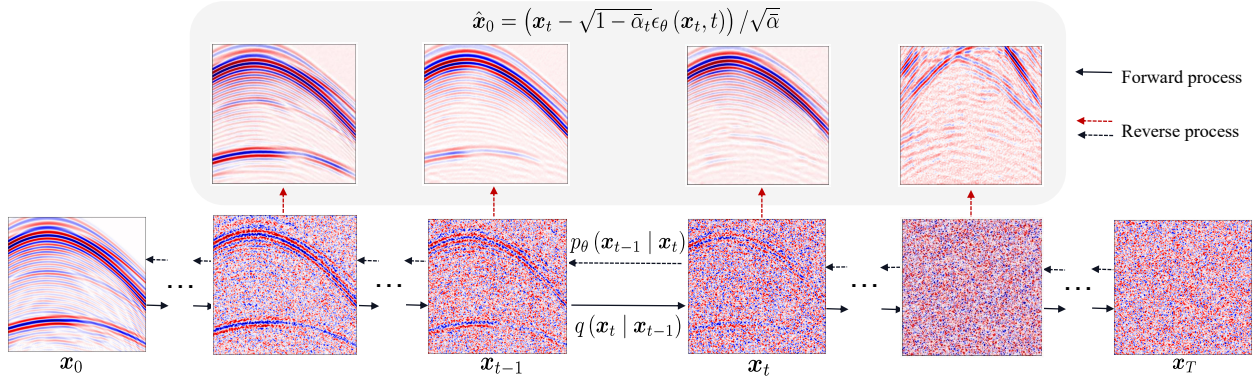


Fig. 1. The pipeline of the seismic DDPM. It comprises two stages, i.e., the forward process and the reverse process. The forward process fixedly converts the complete seismic data \mathbf{x}_0 into a series of noise-added seismic data until \mathbf{x}_T converges to an isotropic Gaussian noise, and the reverse process performs uses the neural network to learn the distribution parameters of each time step. Then \mathbf{x}_0 can be obtained by step-by-step iterative denoising. Especially, \mathbf{x}_0 can also be estimated at each reverse time step and denoted as $\hat{\mathbf{x}}_0$.

data interpolation aims to learn a function mapping observed seismic data \mathbf{y} back to complete data, which is usually implemented by a neural network parameterized by θ . Different from a single neural network model, the diffusion model-based approach incorporates multiple parameterization processes to achieve stepwise approximation. The proposed SeisDDIMR model consists of two main processes, i.e., the training process for estimating the parameters of seismic DDPM and the inference process for interpolating missing seismic data. In Section II-A, we introduce the key principles of DDPM combined with the background of seismic data interpolation. The following Sections, II-B and II-C, provide descriptions of the noise matching network and its corresponding noise schedule. Finally, the inference method, together with its theoretical background, is presented in Section II-D.

A. Seismic Denoising Diffusion Probabilistic Model

Given the complete seismic data samples $\mathbf{x}_0 \sim q(\mathbf{x}_0)$, DDPM relies on the generative Markov chain process and the noise matching network to gradually learn the target distribution $p_\theta(\mathbf{x}_0)$. The forward diffusion process is a deterministic Markov chain starting from the initial input \mathbf{x}_0 and using a pre-specified noise schedule to gradually add Gaussian noise to perturb the data distribution. Given the latent variables $\mathbf{x}_1, \dots, \mathbf{x}_T$ derived from the same sample space with \mathbf{x}_0 , the diffusion process is defined as

$$q(\mathbf{x}_{1:T} | \mathbf{x}_0) := \prod_{t=1}^T q(\mathbf{x}_t | \mathbf{x}_{t-1}), \quad (1)$$

where

$$q(\mathbf{x}_t | \mathbf{x}_{t-1}) := \mathcal{N}(\mathbf{x}_t; \sqrt{1 - \beta_t} \mathbf{x}_{t-1}, \beta_t \mathbf{I}). \quad (2)$$

Here, $\beta_t \in (0, 1)$ is a pre-designed increasing variance schedule of Gaussian noise. The closed form of sampling \mathbf{x}_t given by Ho *et al.* [36] reveals the progressive changes during the middle time of the forward process. Letting $\alpha_t := 1 - \beta_t$ and $\bar{\alpha}_t := \prod_{s=1}^t \alpha_s$, it can be denoted as

$$q(\mathbf{x}_t | \mathbf{x}_0) = \mathcal{N}(\mathbf{x}_t; \sqrt{\bar{\alpha}_t} \mathbf{x}_0, (1 - \bar{\alpha}_t) \mathbf{I}). \quad (3)$$

As t continues to increase, the final data distribution converges to a given prior distribution, i.e., a standard Gaussian for \mathbf{x}_0 . Correspondingly, the reverse process will gradually denoise for each step of the forward process starting from $p(\mathbf{x}_T) = \mathcal{N}(\mathbf{x}_T; \mathbf{0}, \mathbf{I})$ under the Markov chain transition

$$p_\theta(\mathbf{x}_{0:T}) := p(\mathbf{x}_T) \prod_{t=1}^T p_\theta(\mathbf{x}_{t-1} | \mathbf{x}_t), \quad (4)$$

where $p_\theta(\mathbf{x}_{t-1} | \mathbf{x}_t) := \mathcal{N}(\mathbf{x}_{t-1}; \boldsymbol{\mu}_\theta(\mathbf{x}_t, t), \boldsymbol{\Sigma}_\theta(\mathbf{x}_t, t))$ and the network parameter θ is shared across different reverse stages. This optimization problem of fitting the data distribution $q(\mathbf{x}_0)$ can be converted into the minimization of a variational lower bound (VLB) for the negative log likelihood by introducing Jensen's inequality

$$L_{\text{vlb}} := \mathbb{E}_{q(\mathbf{x}_{0:T})} \left[\log \frac{q(\mathbf{x}_{1:T} | \mathbf{x}_0)}{p_\theta(\mathbf{x}_{0:T})} \right] \geq -\mathbb{E}_{q(\mathbf{x}_0)} \log p_\theta(\mathbf{x}_0). \quad (5)$$

VLB is decomposed into the following KL-divergence form between two Gaussian distributions by including the Markov property in the denoising diffusion model and the definition form of the forwards process

$$L_{\text{vlb}} = \mathbb{E}_q [D_{\text{KL}}(q(\mathbf{x}_T | \mathbf{x}_0) \| p(\mathbf{x}_T))] - \mathbb{E}_q [\log p_\theta(\mathbf{x}_0 | \mathbf{x}_1)] + \mathbb{E}_q \left[\sum_{t=2}^T D_{\text{KL}}(q(\mathbf{x}_{t-1} | \mathbf{x}_t, \mathbf{x}_0) \| p_\theta(\mathbf{x}_{t-1} | \mathbf{x}_t)) \right]. \quad (6)$$

According to Ho *et al.* [36], the Gaussian distribution $q(\mathbf{x}_{t-1} | \mathbf{x}_t, \mathbf{x}_0)$ can be tractable as

$$q(\mathbf{x}_{t-1} | \mathbf{x}_t, \mathbf{x}_0) = \mathcal{N}(\mathbf{x}_{t-1}; \tilde{\boldsymbol{\mu}}_t(\mathbf{x}_t, \mathbf{x}_0), \tilde{\beta}_t \mathbf{I}),$$

where

$$\tilde{\boldsymbol{\mu}}_t(\mathbf{x}_t, \mathbf{x}_0) := \frac{\sqrt{\bar{\alpha}_{t-1}} \beta_t}{1 - \bar{\alpha}_t} \mathbf{x}_0 + \frac{\sqrt{\bar{\alpha}_t} (1 - \bar{\alpha}_{t-1})}{1 - \bar{\alpha}_t} \mathbf{x}_t$$

and

$$\tilde{\beta}_t := \frac{1 - \bar{\alpha}_{t-1} \beta_t}{1 - \bar{\alpha}_t}. \quad (7)$$

Furthermore, the first term in Eq. (6) can be ignored as a constant. The discrete probability density of the

second term can be estimated using continuous Gaussian distribution. Combined with the property Eq. (3), $D_{\text{KL}}(q(\mathbf{x}_{t-1} | \mathbf{x}_t, \mathbf{x}_0) || p_\theta(\mathbf{x}_{t-1} | \mathbf{x}_t))$ in the third term of Eq. (6) is simplified to

$$\mathbb{E} \left[\frac{1}{2\sigma_t^2} \left\| \frac{1}{\sqrt{\alpha_t}} \left(\mathbf{x}_t(\mathbf{x}_0, \epsilon_t) - \frac{\beta_t}{\sqrt{1-\bar{\alpha}_t}} \epsilon_t \right) - \boldsymbol{\mu}_\theta(\mathbf{x}_t(\mathbf{x}_0, \epsilon_t), t) \right\|^2 \right],$$

where the constant is omitted and $\epsilon_t \sim \mathcal{N}(\mathbf{0}, \mathbf{I})$. Noting the availability of \mathbf{x}_t , Ho *et al.* [36] transfer the predictions about $\boldsymbol{\mu}_\theta$ to ϵ_θ by the following parameterization

$$\boldsymbol{\mu}_\theta(\mathbf{x}_t, t) = \frac{1}{\sqrt{\alpha_t}} \left(\mathbf{x}_t - \frac{\beta_t}{\sqrt{1-\bar{\alpha}_t}} \epsilon_\theta(\mathbf{x}_t, t) \right). \quad (8)$$

Regardless of the coefficients, since they find that removing them benefits sample quality, the popular loss used in DDPM is finally formulated as

$$L_{\text{simple}} = \mathbb{E}_{\mathbf{x}_0 \sim q(\mathbf{x}_0), \epsilon_t \sim \mathcal{N}(\mathbf{0}, \mathbf{I})} \left[\left\| \epsilon_t - \epsilon_\theta(\sqrt{\alpha_t} \mathbf{x}_0 + \sqrt{1-\bar{\alpha}_t} \epsilon_t, t) \right\|^2 \right]. \quad (9)$$

Therefore, the network parameters are optimized by the mean squared error (MSE) loss between the Gaussian noise predicted by the network and the real noise for all time nodes of the reverse process except for $t = 1$. Moreover, as discussed in [39], the log-likelihood can be improved in the log domain by parameterizing the variance $\boldsymbol{\Sigma}_\theta(\mathbf{x}_t, t) = \sigma_t^2 \mathbf{I}$ with the following interpolation between β_t and $\tilde{\beta}_t$

$$\boldsymbol{\Sigma}_\theta(\mathbf{x}_t, t) = \exp \left(v \log \beta_t + (1-v) \log \tilde{\beta}_t \right),$$

where v can be concatenated on another channel of $\epsilon_\theta(\mathbf{x}_t, t)$, serving as the output of the model. Finally, the loss function of our model is set to

$$L_{\text{hybrid}} = L_{\text{simple}} + \lambda L_{\text{vib}}, \quad (10)$$

where we follow the setting in [39] and adopt $\lambda = 0.001$ to avoid L_{vib} overwhelming L_{simple} . Once the training accomplished, sampling \mathbf{x}_{t-1} from $p_\theta(\mathbf{x}_{t-1} | \mathbf{x}_t)$ can be conducted with the following iterative update formula

$$\mathbf{x}_{t-1} = \frac{1}{\sqrt{\alpha_t}} \left(\mathbf{x}_t - \frac{1-\alpha_t}{\sqrt{1-\bar{\alpha}_t}} \epsilon_\theta(\mathbf{x}_t, t) \right) + \sigma_t \mathbf{z}, \quad (11)$$

where $\mathbf{z} \sim \mathcal{N}(\mathbf{0}, \mathbf{I})$ ($t > 1$) or $\mathbf{z} = \mathbf{0}$ ($t = 1$). Fig. 1 illustrates the detailed stream of the seismic DDPM. The forward process does not require training and directly converts \mathbf{x}_0 to the isotropic Gaussian noise. In the reverse process, the denoising model learns to predict the added noise for each time step. When gradually fitting the noise, the estimated value of \mathbf{x}_0 can also be obtained at each time step according to

$$\hat{\mathbf{x}}_0 = \sqrt{\frac{1}{\alpha_t}} \mathbf{x}_t - \sqrt{\frac{1-\bar{\alpha}_t}{\bar{\alpha}_t}} \epsilon_\theta(\mathbf{x}_t, t), \quad (12)$$

even though it may not be satisfactory during mid-time stamps.

B. Noise Matching Network

The noise matching network used in [36] is based on the U-Net architecture with self-attention [40] and achieves impactful performance. Durall *et al.* [41] adopt this architecture to accomplish seismic data demultiple, denoising, and interpolation. Different from the aforementioned research works, we use a

more appropriate network structure for seismic data generation, whose major stream inherits from the guided-diffusion model [42]. It adopts more architecture improvements to attain better generative quality. The overall architecture is displayed in Fig. 2 using stacked residual blocks (Res Block) and attention blocks (Attn Block and MidAttn Block) for the encoder and decoder of U-Net. \mathbf{x}_t is used as the network input for the denoising learning process to obtain predicted noise $\epsilon_\theta(\mathbf{x}_t, t)$, and the accompanying timestamp t is fed to each layer to embed time information by using the following Transformer sinusoidal time embedding (TE) [40]

$$TE_{(t, 2i)} = \sin \left(t/10000^{2i/d} \right) \\ TE_{(t, 2i+1)} = \cos \left(t/10000^{2i/d} \right),$$

where d stands for the dimension of embedding vectors, t is the original time, and i is the dimension. Figuratively speaking, it serves for \mathbf{x}_t to inform each layer about the current step of reverse diffusion.

Fig. 3a displays the detailed components of the Res Block, Attn Block, and MidAttn Block from left to right, where $N = 2$ for the encoding process and $N = 3$ for the decoding process. Upsampling and downsampling are executed after Res Block and Attn Block, except for the bottom layer, for a total of four operations. As illustrated in Fig. 3b, the residual module is implemented with the inclusion of temporal information within. The MHSA module existing in Attn Block and MidAttn Block increases the receptive field of the model so that it can access all of the input seismic signals as introduced in [40]. Fig. 4 makes a detailed illustration of the MHSA module, which receives the feature map as input and conducts three different linear operations \mathbf{W}_q , \mathbf{W}_k , and \mathbf{W}_v to get the query matrix \mathbf{Q} , key matrix \mathbf{K} , and value matrix \mathbf{V} . Each of them is divided into multiple heads, allowing the model to perform parallel computing and capture relevant information from different subspaces to integrate multiple attentions with different focuses. Self-attention is employed on the branches of each head to learn long-range correlations, which are formulated as

$$\text{Head}_i = \text{Attention}(\mathbf{Q}_i, \mathbf{K}_i, \mathbf{V}_i) = \text{softmax} \left(\frac{\mathbf{Q}_i \mathbf{K}_i^T}{\sqrt{d_k}} \right) \mathbf{V}_i,$$

where d_k is the dimension of queries and keys, and i stands for the number index of heads within $\{1, \dots, N_{\text{head}}\}$. We use $N_{\text{head}} = 4$ in the noise matching network. Finally, MHSA is obtained by integrating the attention of each head together as

$$\text{MHSA}(\mathbf{Q}, \mathbf{K}, \mathbf{V}) = \text{Concat}(\text{Head}_1, \dots, \text{Head}_{N_{\text{head}}}).$$

C. Cosine Noise Schedule

DDPM [36] applies the linear noise schedule for β , where noise increases at a constant rate as the diffusion process proceeds. Since the primary concern in seismic data interpolation is the fidelity of the generated signal, as opposed to diversity, expediting the transition through the stage of high noise can

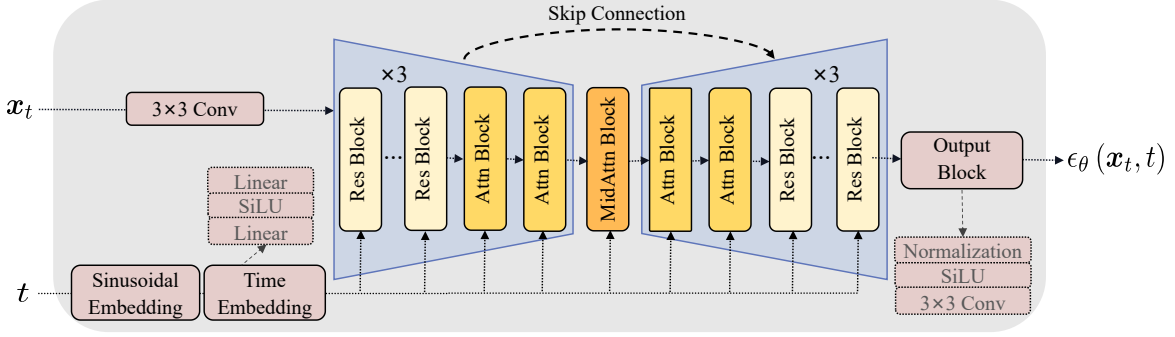


Fig. 2. The overall architecture of the noise matching network. At each step, the network takes in the noise sample \mathbf{x}_t and its corresponding timestamp t as input, and produces the predicted noise $\epsilon_\theta(\mathbf{x}_t, t)$ as output. The main structure of the network is based on U-Net. The inputs \mathbf{x}_t and t are processed separately through convolution and time embedding to have the same dimension, and are then inputted together into the first layer of the network. The detailed structure of the time embedding and output block is displayed at the location indicated by the dashed arrow lines.

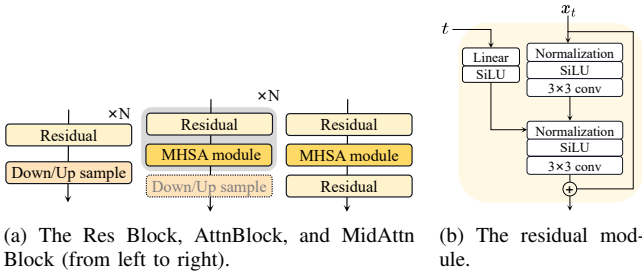


Fig. 3. Residual blocks and attention blocks.

facilitate the reconstruction of unknown areas. We adopt the following cosine schedule [39]

$$\bar{\alpha}_t = \frac{f(t)}{f(0)}, \quad f(t) = \cos\left(\frac{t/T + s}{1 + s} \cdot \frac{\pi}{2}\right)^2,$$

where the offset $s = 0.008$ is used to prevent β_t from being too small near $t = 0$. The gray and blue dots in Fig. 5a display the changing trend of $\bar{\alpha}_t$ in the training process. Compared with the linear noise schedule, the cosine noise schedule can decelerate the global rate of information decay. Meanwhile, the gray dots in Fig. 5b show the changing trend of β_t with respect to diffusion steps during the training process. The reduction of the strong noise states is observable, and it can aid in the interpolation of missing locations. To intuitively observe the differences between the generation processes of different noise schedules, Fig. 6 illustrates the seismic data interpolation results $\hat{\mathbf{x}}_0$ at some middle timestamps during the reverse diffusion process. The interpolated content at intermediate timestamps under the linear noise schedule may deviate significantly from the ground truth distribution in Fig. 6a. In contrast, the differences in distribution between each timestamp are much smaller under the cosine noise schedule, as shown in Fig. 6b. This phenomenon occurs since the cosine noise schedule quickly passes through the high noise phase. Increased availability of known valid information facilitates the generation of missing regions, ensuring consistent alignment between the interpolated content and the ground truth.

D. Implicit Conditional Interpolation with Resampling

The trained seismic DDPM operates unconditionally, wherein the inverse diffusion process is generated directly from noise. However, for seismic data interpolation, it is essential to infer unknown signals from known regions. Hence, further refinement of the interpolation process is necessary. Inspired by the RePaint model [38], we redesign the interpolation process to improve computation feasibility and interpolation quality. Different from the Seismic DDPM used in the training process, the inference process no longer satisfies the Markov assumption, and we adopt the DDIM sampling strategy to mitigate the computation burden existing in the RePaint model.

Intuitively, it seems that the loss function of DDPM ultimately only depends on $q(\mathbf{x}_t | \mathbf{x}_0)$ and the sampling process is only related to $p(\mathbf{x}_{t-1} | \mathbf{x}_t)$, from which Song *et al.* [37] get inspiration for proposing denoising diffusion implicit models (DDIM). They introduce the following non-Markovian inference

$$q_\sigma(\mathbf{x}_{1:T} | \mathbf{x}_0) := q_\sigma(\mathbf{x}_T | \mathbf{x}_0) \prod_{t=2}^T q_\sigma(\mathbf{x}_{t-1} | \mathbf{x}_t, \mathbf{x}_0), \quad (13)$$

with a real vector $\sigma = (\sigma_1, \dots, \sigma_T) \in \mathbb{R}_{\geq 0}$. They choose

$$q_\sigma(\mathbf{x}_{t-1} | \mathbf{x}_t, \mathbf{x}_0) = \mathcal{N}\left(\sqrt{\bar{\alpha}_{t-1}}\mathbf{x}_0 + \sqrt{1 - \bar{\alpha}_{t-1} - \sigma_t^2} \cdot \frac{\mathbf{x}_t - \sqrt{\bar{\alpha}_t}\mathbf{x}_0}{\sqrt{1 - \bar{\alpha}_t}}, \sigma_t^2 \mathbf{I}\right) \quad (14)$$

to ensure $q_\sigma(\mathbf{x}_t | \mathbf{x}_0)$ remains consistent with the form in Eq. (3). Under the above definition, the forward process $q_\sigma(\mathbf{x}_t | \mathbf{x}_{t-1}, \mathbf{x}_0)$ is still rebuilt as Gaussian and the VLB can then be written as

$$\begin{aligned} L_{\text{VLB}}^\sigma &:= \mathbb{E}_{\mathbf{x}_{0:T} \sim q_\sigma(\mathbf{x}_{0:T})} [\log q_\sigma(\mathbf{x}_{1:T} | \mathbf{x}_0) - \log p_\theta(\mathbf{x}_{0:T})] \\ &= \mathbb{E}_{\mathbf{x}_{0:T} \sim q_\sigma(\mathbf{x}_{0:T})} \left[\log q_\sigma(\mathbf{x}_T | \mathbf{x}_0) + \sum_{t=2}^T \log q_\sigma(\mathbf{x}_{t-1} | \mathbf{x}_t, \mathbf{x}_0) \right] \\ &\quad - \mathbb{E}_{\mathbf{x}_{0:T} \sim q_\sigma(\mathbf{x}_{0:T})} \left[\sum_{t=1}^T \log p_\theta^{(t)}(\mathbf{x}_{t-1} | \mathbf{x}_t) - \log p_\theta(\mathbf{x}_T) \right]. \end{aligned}$$

Song *et al.* [37] have proved that the objective function, i.e., Eq. (9), ultimately used by DDPM is a special case of L_{VLB}^σ under certain conditions, which allows us to directly

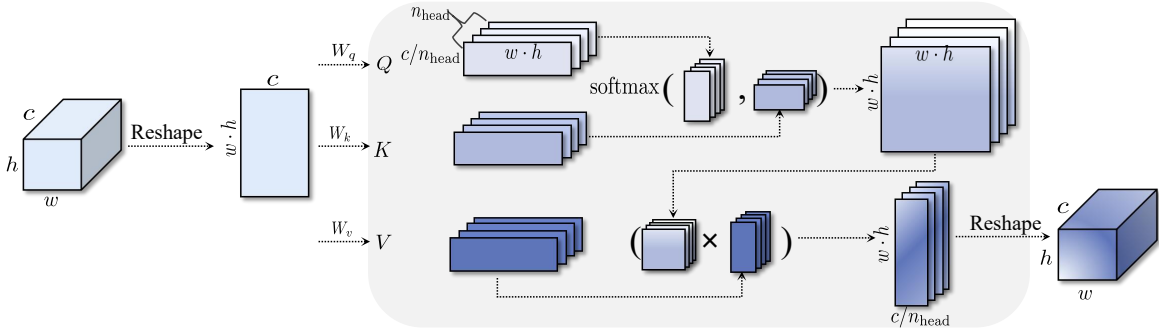


Fig. 4. MHSA module

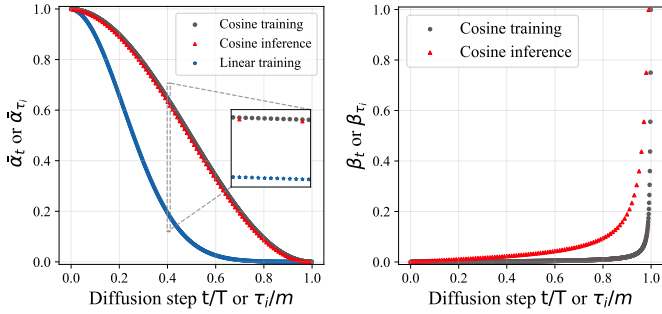

 (a) The changing trend of α_t versus the step of diffusion. (b) The changing trend of β_t versus the step of diffusion.

Fig. 5. Noise schedule in the training and inference process

use the pre-trained DDPM model as a solution for new objectives. With the aforementioned theoretical foundation, sampling from this non-Markovian generative process is focused on constructing σ to improve sample generation and reduce sample steps. Starting from Eq. (14), the sampling operation can be formulated as

$$\mathbf{x}_{t-1} = \sqrt{\bar{\alpha}_{t-1}} \left(\frac{\mathbf{x}_t - \sqrt{1 - \bar{\alpha}_t} \epsilon_\theta(\mathbf{x}_t, t)}{\sqrt{\bar{\alpha}_t}} \right) + \sqrt{1 - \bar{\alpha}_{t-1} - \sigma_t^2} \cdot \epsilon_\theta(\mathbf{x}_t, t) + \sigma_t \mathbf{z}, \quad (15)$$

where the generative process becomes Markovian and equals DDPM if $\sigma_t = \sqrt{(1 - \bar{\alpha}_{t-1}) / (1 - \bar{\alpha}_t)} \sqrt{1 - \bar{\alpha}_t / \bar{\alpha}_{t-1}}$ for all t . Especially, it is reasonable to consider a sampling process of length less than T when $q_\sigma(\mathbf{x}_t | \mathbf{x}_0)$ is fixed since the optimization result of DDPM essentially contains its optimization results for arbitrary subsequence parameters. Denoting the increasing time subsequence of the original time sequence $[1, \dots, T]$ as $\tau = [\tau_1, \tau_2, \dots, \tau_m]$ with of length m (the corresponding changes in $\bar{\alpha}_{\tau_i}$ and β_{τ_i} are shown in the red points of Figs. 5a and 5b, respectively), the σ_τ used in accelerated sampling process follows

$$\sigma_{\tau_i}(\eta) = \eta \sqrt{(1 - \bar{\alpha}_{\tau_{i-1}}) / (1 - \bar{\alpha}_{\tau_i})} \sqrt{1 - \bar{\alpha}_{\tau_i} / \bar{\alpha}_{\tau_{i-1}}}, \quad (16)$$

where $\eta \geq 0$. In particular, the generative process is defined as DDIM if $\eta = 0$ for all t since the variance σ keeps zero, so that the deterministic forward process becomes an implicit probabilistic model.

Each step of the iterative reverse diffusion stage in the inference process uses the following implicit conditional interpolation formula

$$\mathbf{x}_{\tau_{i-1}} = \mathbf{m} \odot \mathbf{x}_{\tau_{i-1}}^{\text{valid}} + (1 - \mathbf{m}) \odot \mathbf{x}_{\tau_{i-1}}^{\text{missing}}, \quad (17)$$

where $\mathbf{x}_{\tau_{i-1}}^{\text{valid}}$ is directly sampled from the forward diffusion process, i.e., Eq. (3), which adds known information to the reverse process, and $\mathbf{x}_{\tau_{i-1}}^{\text{missing}}$ is obtained by using the DDIM sampling formula Eq. (15). As a result, $\mathbf{x}_{\tau_{i-1}}$ incorporates information from both known signals and model predicted signals before forwarding it to the next inverse diffusion step. The recovery of missing seismic data is designed as a implicit conditional interpolation process based on valid seismic data.

Merely relying on the known signal as the condition is not adequate. Despite the relationship between the interpolated and known signals, maintaining interpolated signal continuity and consistency with known signals remains challenging. We introduce the resampling strategy [38] to enhance the consistency of sampling in the reverse process. After sampling $\mathbf{x}_{\tau_{i-1}}$ in the inverse diffusion process, the forward diffusion sampling is performed again to generate \mathbf{x}_{τ_i} , with the difference being that \mathbf{x}_{τ_i} now contains the information from $\mathbf{x}_{\tau_{i-1}}^{\text{missing}}$, thereby promoting consistency with known signals. Naturally, this kind of resampling operation cannot be performed only once. We define the jump length, denoted as L , to set how many times to backtrack for each resampling process, and we define the jump height, denoted as H , which determines the interval between time steps before and after two different resampling processes.

In a word, our SeisDDIMR model comprises two key processes, i.e., the seismic DDPM training process and the implicit conditional interpolation process with resampling. Algorithm 1 and Algorithm 2 list the overview of our training and inference procedure, respectively.

III. EXPERIMENTS

A. Evaluation Metrics

We choose three metrics, i.e., MSE, signal-to-noise ratio (SNR), and peak signal-to-noise ratio (PSNR), to compare the fidelity of the interpolated seismic data. MSE between the interpolated seismic data $\{\hat{\mathbf{x}}^j\}_{j=1}^n$ and the ground truth $\{\mathbf{x}_{\text{gt}}^j\}_{j=1}^n$ is calculated using

$$\text{MSE} = \frac{1}{n} \sum_{j=1}^n (\hat{\mathbf{x}}^j - \mathbf{x}_{\text{gt}}^j)^2,$$

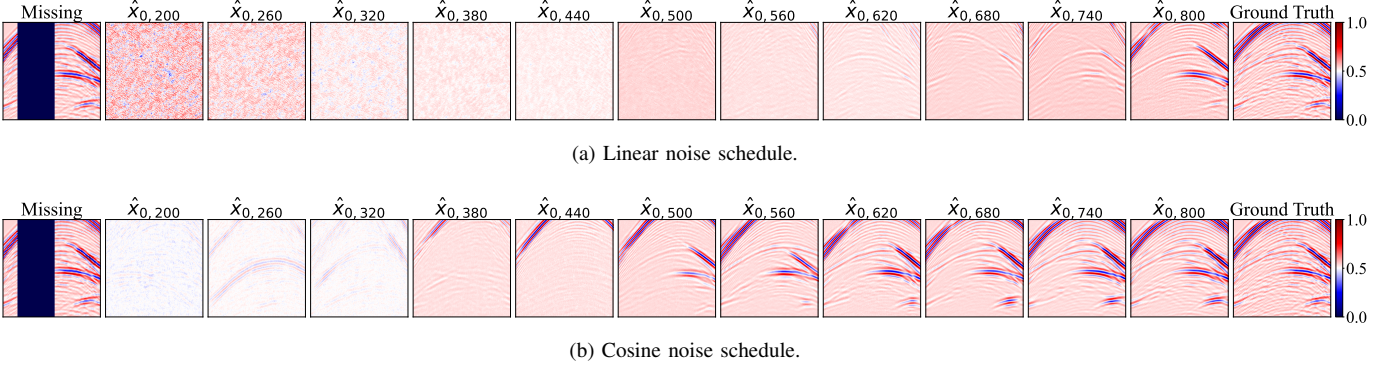


Fig. 6. Seismic interpolation visualization in the reverse diffusion process with different noise schedules.

Algorithm 1 Training Seismic DDPM

Input: Complete training data $\{x_0^i\}_{i=1}^n$ with total number n ; Specifying the parameters of DDPM, i.e., diffusion steps T ; Batch size K ; The number of iterations N .

- 1: Randomly initialize the noise matching network;
 - 2: **for** $j = 1, \dots, N$ **do**
 - 3: Sample batch data $\{x_0^i\}_{i=1}^K$ from training data;
 - 4: Sample $\{t_i\}_{i=1}^K$ from $\text{Uniform}(\{1, \dots, T\})$;
 - 5: Sample $\{\epsilon_{t_i}\}_{i=1}^K$ from $\mathcal{N}(\mathbf{0}, \mathbf{I})$;
 - 6: Get $\{\epsilon_{\theta}(x_{t_i}^i, t_i)\}_{i=1}^K$ from the noise matching network;
 - 7: Update the noise matching network with L_{hybrid} ;
 - 8: **end for**
-

where its value closer to 0 implies a higher fidelity of the interpolation result. The SNR for a single interpolated sample is defined as

$$\text{SNR} = 10 \log_{10} \frac{\|x_{\text{gt}}\|_F^2}{\|x_{\text{gt}} - \hat{x}\|_F^2},$$

where $\|\cdot\|_F$ represents the Frobenius norm. PSNR is calculated by the following formula as

$$\text{PSNR} = 10 \log_{10} \frac{\text{MAX}_{x_{\text{gt}}}^2}{\text{MSE}},$$

where $\text{MAX}_{x_{\text{gt}}}$ refers to the highest value of x_{gt} . Obviously, larger SNR and PSNR both symbolize higher interpolation fidelity. The quality of the texture of the interpolation is evaluated using structural similarity (SSIM) [43], which is widely used in the field of image generation following the formula

$$\text{SSIM}(x_{\text{gt}}, \hat{x}) = L(x_{\text{gt}}, \hat{x}) \cdot C(x_{\text{gt}}, \hat{x}) \cdot S(x_{\text{gt}}, \hat{x}).$$

Separately, $L(\cdot)$, $C(\cdot)$, and $S(\cdot)$ indicate similarities in luminance, contrast, and structure, and they are each defined as

$$L(x_{\text{gt}}, \hat{x}) = \frac{2\mu_{x_{\text{gt}}}\mu_{\hat{x}} + c_1}{\mu_{x_{\text{gt}}}^2 + \mu_{\hat{x}}^2 + c_1},$$

$$C(x_{\text{gt}}, \hat{x}) = \frac{2\sigma_{x_{\text{gt}}}\sigma_{\hat{x}} + c_2}{\sigma_{x_{\text{gt}}}^2 + \sigma_{\hat{x}}^2 + c_2},$$

$$S(x_{\text{gt}}, \hat{x}) = \frac{\sigma_{x_{\text{gt}}\hat{x}} + c_3}{\sigma_{x_{\text{gt}}}\sigma_{\hat{x}} + c_3},$$

Algorithm 2 Implicit Conditional Interpolation with Resampling

Input: Missing seismic data x_0 ; Corresponding missing mask m ; Trained seismic DDPM model; Specifying the parameters of DDIM, i.e., diffusion sampling steps $\tau = [\tau_1, \tau_2, \dots, \tau_m]$ with length of m ; Jump length L ; Jump height H ;

- 1: $x_{\tau_m}^{\text{missing}} \sim \mathcal{N}(\mathbf{0}, \mathbf{I})$;
- 2: Sample $x_{\tau_m}^{\text{valid}}$ from Eq. (3);
- 3: Get x_{τ_m} from Eq. (17);
- 4: $\tau_i = \tau_m$;
- 5: **while** $\tau_i \geq \tau_1$ **do**
- 6: **for** $h = 1, \dots, H$ **do**
- 7: $\epsilon \sim \mathcal{N}(\mathbf{0}, \mathbf{I})$ if $\tau_i > \tau_1$, else $\epsilon = \mathbf{0}$;
- 8: Sample $x_{\tau_{i-1}}^{\text{valid}}$ from Eq. (3);
- 9: $z \sim \mathcal{N}(\mathbf{0}, \mathbf{I})$ if $\tau_i > \tau_1$, else $z = \mathbf{0}$;
- 10: Get $x_{\tau_{i-1}}^{\text{missing}}$ from Eq. (15);
- 11: Get $x_{\tau_{i-1}}$ from Eq. (17), $\tau_i = \tau_{i-1}$;
- 12: **end for**
- 13: **if** $\tau_i \geq \tau_1$ **then**
- 14: **for** $l = 1, \dots, L$ **do**
- 15: Repeat 6-12;
- 16: **for** $h = 1, \dots, H$ **do**
- 17: Get \hat{x}_0 from Eq. (12), $\tau_i = \tau_{i+1}$;
- 18: Sample x_{τ_i} from Eq. (3), where $x_0 = \hat{x}_0$;
- 19: **end for**
- 20: **end for**
- 21: **end if**
- 22: **end while**

Output: Interpolated data x_{τ_1} .

where $\mu_{x_{\text{gt}}}(\mu_{\hat{x}})$, $\sigma_{x_{\text{gt}}}(\sigma_{\hat{x}})$, and $\sigma_{x_{\text{gt}}\hat{x}}$ denote the mean value and standard deviation, and covariance, respectively. Constants c_1 , c_2 , and c_3 are typically set close to zero to prevent numerical instability. Thus, a higher SSIM implies a more similar texture.

B. Data Set

We validate our method over one open synthetic dataset provided by the Society of Exploration Geophysicists (SEG) C3 and one field dataset Mobil Avo Viking Graben Line 12 (MAVO). The SEG C3 dataset consists of 45 shots, each with

a 201×201 receiver grid, 625 time samples per trace, and a sampling interval of 8 ms. We randomly extract 35,000 128×128 patches, out of which 25,000 patches are utilized for training, 5,000 for validation, and another 5,000 for testing. MAVO dataset comprises a 1001×120 receiver grid with 1500 time samples per trace. It is collected at a time rate of 4 ms and a spatial rate of 25 m. We randomly extract 10,000 256×112 patches, with 6,000 used for training, 2,000 used for validation, and 2,000 used for testing. All seismic patches are firstly normalized within the interval $[0, 1]$ by applying min-max normalization.

C. Implementation Details

The diffusion step for the Seismic DDPM model is set to 1000. We train the seismic DDPM model on the training sets of SEG C3 and MAVO separately, as described in Algorithm 1, with N iterations of 600,000 and 300,000, respectively. The noise matching network is optimized by AdamW with a learning rate of $1e-4$. The batch size is set to 30 for the SEG C3 dataset and 15 for the MAVO dataset. Our SeisDDIMR test is conducted by using Algorithm 2, where we adopt diffusion sampling step $m = 100$, jump length $L = 10$, and jump height $H = 1$. We compare our experimental results with 5 currently popular methods, including DD-CGAN [32], cWGAN-GP [33], PConv-UNet [27], ANet [23], and Coarse-to-Fine [34]. All of the experiments are implemented using Pytorch 1.12.1 and NVIDIA GeForce RTX 3090 GPU.

D. Experimental Results

We conduct Algorithm 2 to accomplish our model testing. Interpolation reconstructions are performed on three missing categories of seismic data, and the experimental results are displayed below, followed by a comparison to other methods. It worth noting that our SeisDDIMR model is trained only once on each dataset, whereas other comparison methods are trained multiple times according to various trace missing forms, and the details of the training parameters remain consistent with their respective original papers.

1) *Random Missing Traces*: For each patch in the test sets of SEG C3 and MAVO, we design random missing phenomena with missing rates ranging from 0.2 to 0.6. The initial values of the missing traces are set to 0. The experimental results of random missing interpolation are listed on the left side of Tab. I and Tab II. Except for being slightly inferior in the SSIM, the other three metrics demonstrate that our model has better fidelity. Fig. 7 shows the interpolated traces of the random missing MAVO test data. It can be seen that our method achieves the best performance both on amplitudes and phases. As a special case of random missing seismic data, the regular missing scenario will cause a serious aliasing problem. It usually appears as excessive artifacts in the high-frequency band of $f-k$ spectra caused by erroneous estimation or interpolation of the missing data frequency. Fig. 8 compares the $f-k$ spectra of SEG C3 test data with 70% regular missing traces. Severe aliasing can be noticed in Fig. 8d. It is obvious that the $f-k$ spectra of the DD-CGAN, cWGAN-G, and ANet are all accompanied by significant high-frequency artifacts.

Comparisons between the performance of all methods indicate that our model gains the most consistent $f-k$ spectra with the ground truth.

2) *Consecutive Missing Traces*: We randomly create consecutive missing masks, with rates of missing data ranging from 0.1 to 0.4 (not including edge traces), and applied them to the patches in the SEG C3 and MAVO datasets. The value of missing traces is initialized to 0. The interpolation results of the middle four columns of Tab. I and Tab. II indicate that our model consistently surpasses other methods over these two datasets. we provide the comparisons via color plots from the SEG C3 test dataset as in Fig. 9. The ground truth data suffers from a consecutive missing of 40% resulting in degenerate missing data. Significant differences in the distribution are visible in the known portions on either side, which hinder the ability of some methods, such as PConv-UNet and ANet, that rely solely on feature similarity to perform the interpolation. DD-CGAN, cWGAN-GP, and Coarse-to-Fine methods based on GAN are still limited in their interpolation ability and tend to smooth small-scale seismic events due to large interval problems. Among these, cWGAN-GP demonstrates a high continuity in strong amplitude regions with biasedly sacrificing the performances on the fidelity of weak amplitudes. Coarse-to-Fine acquires fine details of weak amplitudes but it still exhibits significant differences from the ground truth data. Our model can consistently improve the performances over both strong and weak amplitudes, and keep anisotropy and spatial continuity of signals.

3) *Multiple Missing Traces*: For the SEG C3 and MAVO datasets, we construct multiple missing data scenarios with both consecutive and random missing cases and the range of the total missing rate is $[0.2, 0.8]$. The missing traces are also initialized with a value of 0. The corresponding quantitative comparison results are listed in the right four columns of Tab. I and Tab. II, where our model consistently outperforms other methods on four metrics. Fig. 10 exhibits the interpolation results on a multiple missing example with total missing rare 54% from the MAVO test data. Our model produces artifact-free results, while other methods generally result in the ubiquity wide areas of artifacts, especially for DD-CGAN, cWGAN-G, and PConv-UNet, failing to provide reliable recovery. In addition, the amplitudes predicted by our model are more accurate and consistent with the ground truth. Our model is capable of handling most cases of seismic missing trace reconstruction.

E. Model Robustness

In order to study the impact of changes in the missing form on model capability, we evaluate the performance of different methods under the unmatched training and testing mask patterns, as shown in Tab. III. First, when testing on the unseen consecutive mask pattern, the performance of the models trained on the random mask type has decreased significantly compared to those consecutive missing reconstruction results in Tab. I. Second, although the model trained on the multiple mask form exhibits interpolation capability on different mask types, their results are still worse than those trained on the

TABLE I
COMPARISON OF DIFFERENT METHODS ON THE TEST SET OF THE SEG C3 DATASET WITH VARIOUS MISSING TYPES. THE BEST PERFORMANCE IS HIGHLIGHTED IN BOLD.

Missing type Model	Random				Consecutive				Multiple			
	MSE↓	SNR↑	PSNR↑	SSIM ↑	MSE↓	SNR↑	PSNR↑	SSIM ↑	MSE↓	SNR↑	PSNR↑	SSIM ↑
DD-CGAN[32]	3.361e-04	29.104	34.735	0.925	7.933e-04	25.374	31.005	0.863	6.385e-04	26.317	31.948	0.875
cWGAN-GP[33]	4.950e-05	37.423	43.054	0.990	2.910e-04	29.729	35.360	0.952	2.813e-04	29.877	35.508	0.953
PConv-UNet[27]	5.235e-05	37.180	42.811	0.991	3.093e-04	29.465	35.096	0.953	2.700e-04	30.055	35.686	0.960
ANet[23]	1.710e-04	32.039	37.670	0.966	4.683e-04	27.664	33.295	0.930	4.413e-04	27.922	33.553	0.934
Coarse-to-Fine[34]	4.608e-05	37.734	43.365	0.991	2.007e-04	31.343	36.974	0.969	1.823e-04	31.761	37.392	0.969
Ours	3.351e-05	39.134	44.765	0.990	9.855e-05	34.499	40.130	0.983	1.516e-04	32.617	38.248	0.976

TABLE II
COMPARISON OF DIFFERENT METHODS ON THE TEST SET OF THE MAVO DATASET WITH VARIOUS MISSING TYPES. THE BEST PERFORMANCE IS HIGHLIGHTED IN BOLD.

Missing type Model	Random				Consecutive				Multiple			
	MSE↓	SNR↑	PSNR↑	SSIM ↑	MSE↓	SNR↑	PSNR↑	SSIM ↑	MSE↓	SNR↑	PSNR↑	SSIM ↑
DD-CGAN[32]	3.723e-04	28.764	34.292	0.928	5.335e-04	27.201	32.729	0.901	6.117e-04	26.607	32.135	0.893
cWGAN-GP[33]	2.024e-04	31.411	36.938	0.968	3.442e-04	29.104	34.632	0.945	3.873e-04	28.592	34.120	0.936
PConv-UNet[27]	1.435e-04	32.904	38.431	0.974	2.705e-04	30.151	35.678	0.954	3.118e-04	29.534	35.062	0.946
ANet[23]	2.529e-04	30.442	35.970	0.961	4.280e-04	28.158	33.685	0.935	4.704e-04	27.747	33.275	0.928
Coarse-to-Fine[34]	1.419e-04	32.954	38.481	0.975	1.959e-04	31.553	37.080	0.965	2.961e-04	29.759	35.286	0.952
Ours	1.190e-04	33.753	39.281	0.971	1.046e-04	34.311	39.839	0.976	2.039e-04	31.437	36.965	0.957

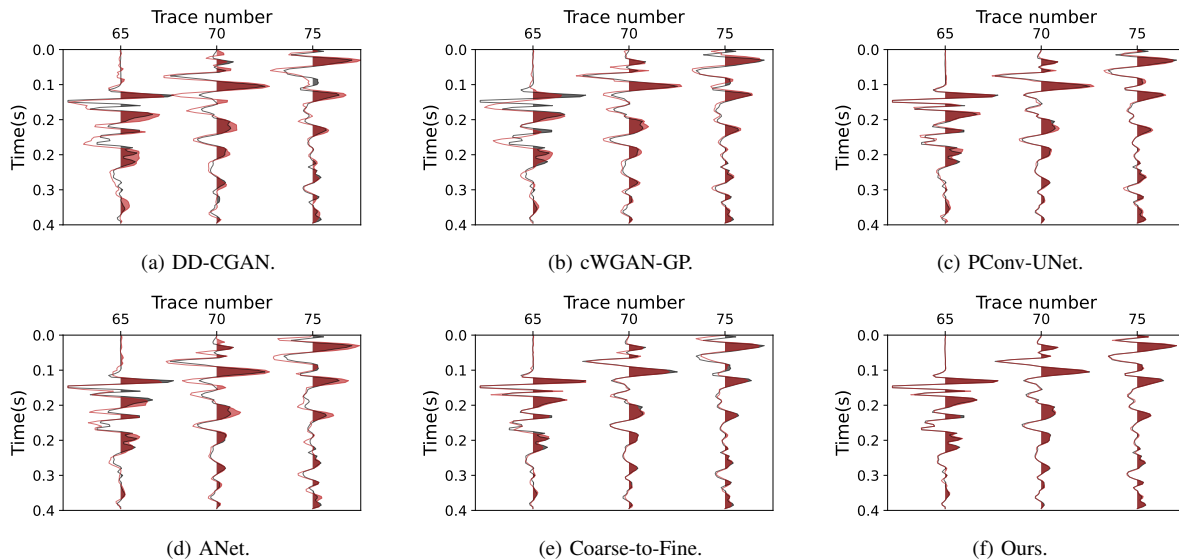


Fig. 7. Interpolation results of MAVO test data with random missing traces on different methods. Several randomly missing traces are chosen in wiggle plots to demonstrate the performance of interpolation, where the red and black wiggly lines represent the interpolation result and the ground truth, respectively.

same mask pattern, as demonstrated in Tab. I. Third, we can see that the consecutive missing model fails to interpolate random missing data, which is likely due to the significant differences in learning patterns between consecutive missing form and random missing form. It can be concluded that the effectiveness of generative models, which may be based on GAN or feature similarity, is sensitive to the constructed mask formula in training data. It seems better if the training missing construction can be closer to the missing form of the test data, although there easily exist gaps in the field scenarios. In contrast, our model training does not require rigorous construction of missing scenes and only needs one training to complete interpolation of any missing form while maintaining advantages in performance.

F. Uncertainty Quantification

Although various interpolation methods based on deep learning have accomplished promising results in the aforementioned publications, uncertainty quantification of the prediction is still absent subjecting to the fixed inference mode. However, providing measures of uncertainty for the predictions over or under confidence is important to improve the application security and avoid the cost of an error. The uncertainty in deep neural networks is divided into the reducible model uncertainty (also systemic or epistemic uncertainty) and irreducible data uncertainty (also statistical or aleatoric uncertainty) [44]. The model uncertainty is caused by inadequate models and unsuitable learning patterns, and data uncertainty is an inherent characteristic of data and cannot be reduced or eliminated by improving the subsequent model.

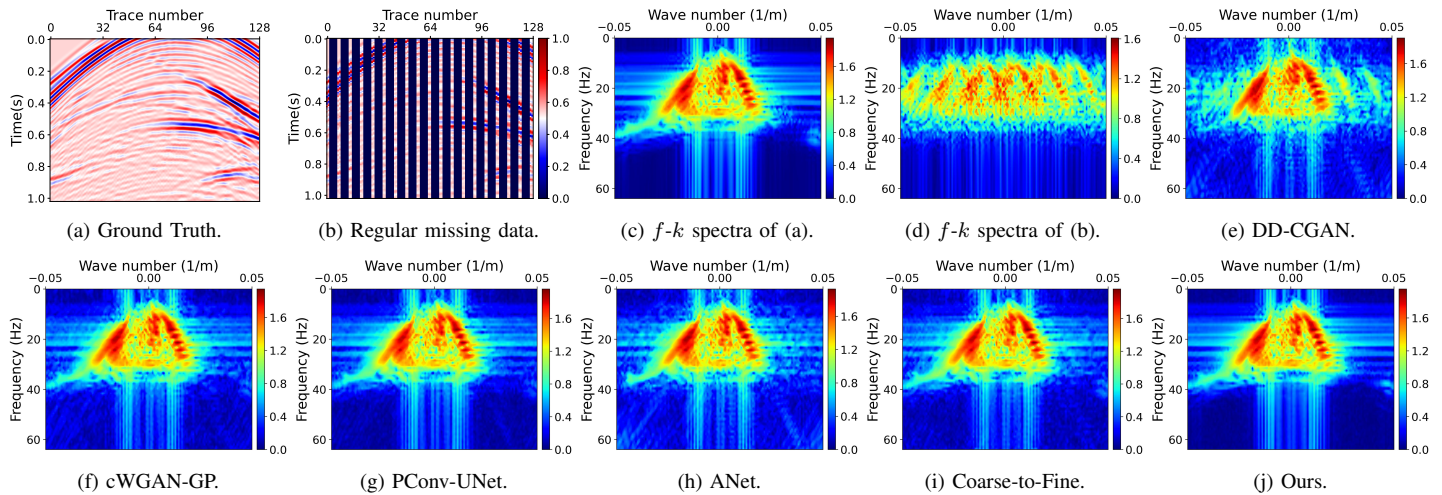


Fig. 8. The f - k spectra of SEG C3 test data interpolation results with 70% regular missing traces on different methods.

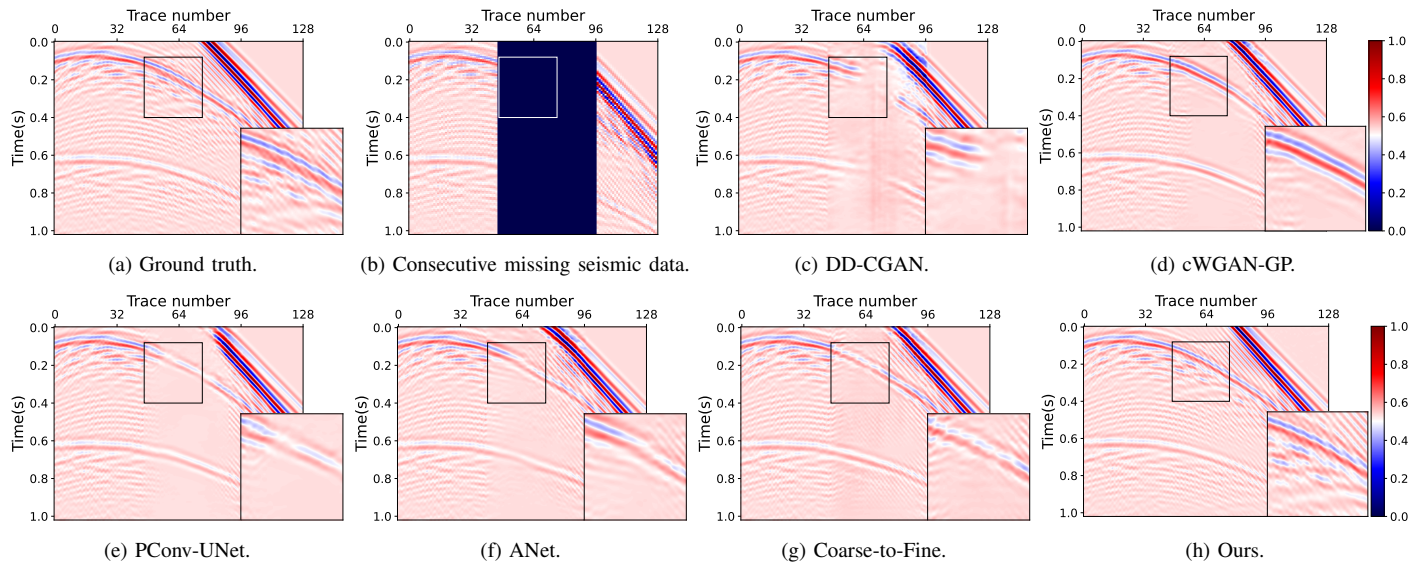


Fig. 9. Interpolation results of SEG C3 test data with 40% consecutive missing traces on different methods. The reconstruction region within the box is magnified in the bottom right corner to allow for a more detailed observation of the interpolation.

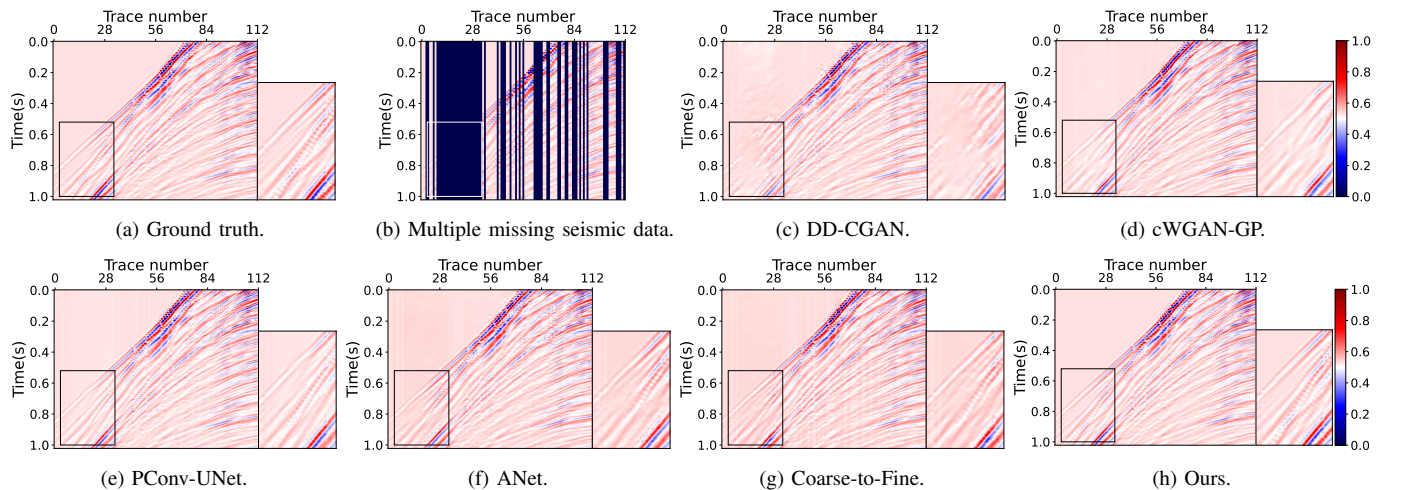


Fig. 10. Interpolation results of MAVO test data with 54% multiple missing types on different methods. To observe the interpolation in more detail, the reconstruction region within the box is magnified on the right side.

TABLE III
ROBUSTNESS COMPARISON OF DIFFERENT MODELS ON THE TEST SET OF THE SEG C3 DATASET UNDER UNMATCHED TRAINING AND TESTING MASK PATTERNS. THE RESULT OF TOP PERFORMANCE IS MASKED IN BOLD.

Type	Model	MSE	SNR	PSNR	SSIM
Random to consecutive	DD-CGAN[32]	1.230e-03	23.471	29.102	0.841
	cWGAN-GP[33]	6.627e-04	26.156	31.787	0.926
	PCConv-UNet[27]	6.851e-04	26.011	31.643	0.926
	ANet[23]	8.167e-04	25.248	30.880	0.908
	Coarse-to-Fine[34]	5.345e-04	27.089	32.720	0.943
Multiple to consecutive	DD-CGAN[32]	1.038e-03	24.207	29.838	0.848
	cWGAN-GP[33]	4.317e-04	28.017	33.648	0.947
	PCConv-UNet[27]	3.557e-04	28.858	34.489	0.951
	ANet[23]	5.597e-04	26.889	32.520	0.923
	Coarse-to-Fine[34]	2.374e-04	30.615	36.246	0.965
	Ours	9.855e-05	34.499	40.130	0.983
Consecutive to random	DD-CGAN[32]	3.077e-02	9.488	15.119	0.511
	cWGAN-GP[33]	6.418e-03	16.295	21.926	0.648
	PCConv-UNet[27]	7.048e-03	15.888	21.520	0.741
	ANet[23]	2.757e-03	19.965	25.596	0.774
	Coarse-to-Fine[34]	3.132e-02	9.410	15.041	0.367
Multiple to random	DD-CGAN[32]	3.888e-04	28.471	34.102	0.906
	cWGAN-GP[33]	7.390e-05	35.683	41.314	0.989
	PCConv-UNet[27]	5.786e-05	36.745	42.376	0.990
	ANet[23]	2.337e-04	30.682	36.314	0.959
	Coarse-to-Fine[34]	5.562e-05	36.917	42.548	0.988
	Ours	3.351e-05	39.134	44.765	0.990

There are multiple random sampling operations in our SeisDDIMR model as stated in Algorithm 2, thus we adopt the approach deriving from uncertainty ensemble methods to capture the total uncertainty by calculating the standard deviation of the interpolation results obtained after multiple repetitions of Algorithm 2. For a sample \mathbf{x} , the uncertainty is computed as

$$\frac{1}{n} \sum_{i=1}^n (\hat{\mathbf{x}}_i - \hat{\mu}_i)^2,$$

where $\hat{\mu}_i = \frac{1}{n} \sum_{i=1}^n \hat{\mathbf{x}}_i$, $\hat{\mathbf{x}}_i$ is the interpolation result of single test, and n is the repetition test number. Fig. 11-13 visualize the uncertainty in the interpolation results of random, consecutive, and multiple missing traces, respectively. The average interpolation results and average residual $\frac{1}{n} \sum_{i=1}^n (\hat{\mathbf{x}}_i - \mathbf{x}_{gt})$ are also exhibited to provide an intuitive reference. It seems that unreliable reconstruction results are more likely to occur in the missing areas with patch edges and strong lateral amplitude variations, due to limited information and highly curved events. Besides, areas with high interpolation uncertainty also acquire large residuals.

IV. ABLATION STUDY

In this section, we will conduct a series of ablation studies on the key components and hyperparameters from three aspects including the MHSA module, seismic DDPM, and implicit interpolation with resampling strategy.

A. MHSA Module

We carry out our model training under different settings in the MHSA module with the total iteration number $N = 300,000$. The ablation study focuses on the location of MHSA in the network and the number of attention heads. Tab. IV lists

the interpolation results on the validation set of SEG C3 data with multiple missing traces, where 32, 16, and 8 represent the resolution of the feature map in the noise matching network, respectively, meaning that the MHSA module is placed on the corresponding layer. We list the optimal configuration and its result on the top row. The following several rows show the results with one of the settings changed. It is evident that the best performance is achieved with the settings of attention head number $N_{\text{head}} = 4$ and attention location = 16, 8.

TABLE IV
ABLATION OF VARIOUS CHANGES OF THE MHSA MODULE. THE RESULT OF THE TOP PERFORMANCE IS MASKED IN BOLD.

N_{head}	MHSA location	MSE	SNR	PSNR	SSIM
4	16,8	1.580e-04	32.487	38.107	0.975
2		1.615e-04	32.031	37.617	0.973
1		1.853e-04	31.740	37.360	0.971
	8	1.730e-04	32.054	37.674	0.974
	32,16,8	1.622e-04	32.323	37.943	0.972
	32,16	1.822e-04	31.821	37.440	0.971

B. Seismic DDPM

The training of the Seismic DDPM is implemented by the process described in Algorithm 1. We selected three key components, i.e., diffusion steps T , loss function, and noise schedule, to validate the superiority of the adopted configuration. Seismic DDPM is trained on the SEG C3 dataset under different settings with the total iteration number $N = 300,000$, respectively. Tab. V yields the interpolation results on the SEG C3 validation dataset with multiple missing traces. First, the number of diffusion steps T has a significant impact on the diffusion speed of our model. Increasing T refines the model, but also causes additional computational burden. Achieving a balance between computational efficiency and model performance requires a compromise configuration of the diffusion steps. Second, Tab. V indicates that better interpolation results can be achieved by allowing the noise matching network to learn the noise variance σ_t under the hybrid loss L_{hybrid} . Finally, training seismic DDPM with different noise schedules indicates that using a linear schedule suffers from significant performance degradation. This finding supports our decision to adopt the cosine schedule, which has demonstrated better performance.

TABLE V
ABLATION OF VARIOUS SETTINGS IN SEISMIC DDPM. THE RESULT OF THE TOP PERFORMANCE IS MASKED IN BOLD.

T	λ	Noise schedule	MSE	SNR	PSNR	SSIM
1000	0.001	Cosine	1.580e-04	32.487	38.107	0.975
500			1.739e-04	32.042	37.661	0.971
100			2.245e-04	30.909	36.529	0.961
	0		2.020e-04	31.380	37.000	0.968
		Linear	2.443e-04	30.529	36.149	0.961

C. Implicit Interpolation with Resampling Strategy

To assess the efficacy of our proposed implicit interpolation and resampling strategy, we execute Algorithm 2 under various

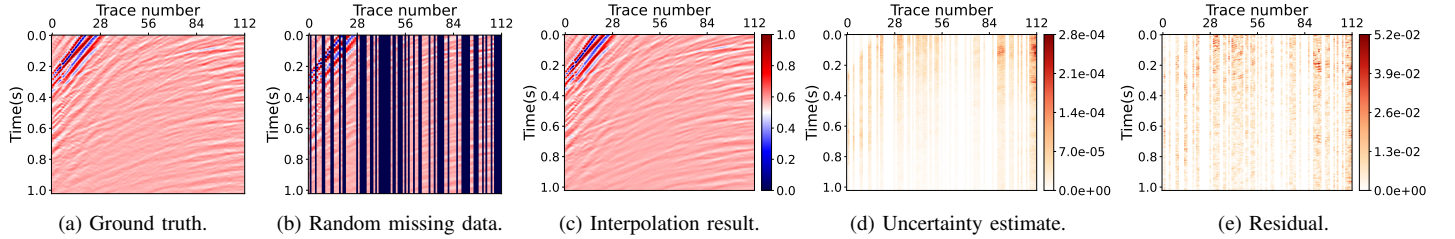


Fig. 11. Uncertainty quantification on the interpolation result of MAVO test data with random missing traces. The interpolation result in (c) is the uncertainty obtained from multiple test repetitions. The absolute value of the average residual is presented in (e) for the comparison purpose.

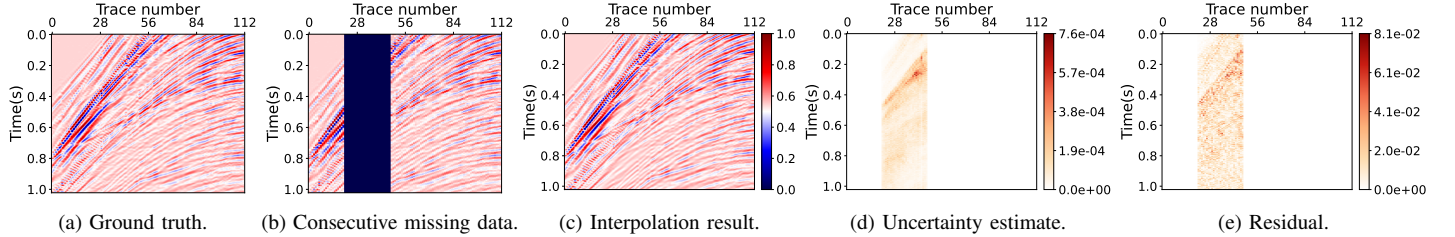


Fig. 12. Uncertainty quantification on the interpolation result of MAVO test data with consecutive missing traces. The interpolation result in (c) is the uncertainty obtained from multiple test repetitions. The absolute value of the average residual is presented in (e) for the comparison purpose.

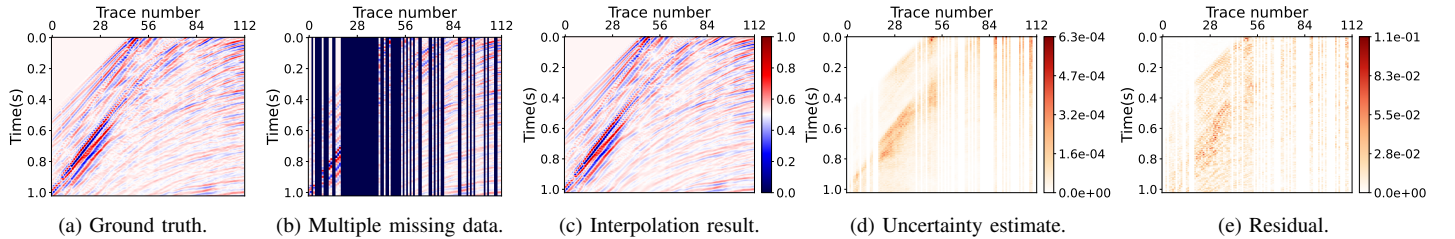


Fig. 13. Uncertainty quantification on the interpolation result of MAVO test data with multiple missing traces. The interpolation result in (c) is the uncertainty obtained from multiple test repetitions. The absolute value of the average residual is presented in (e) for the comparison purpose.

configurations on the validation set of the MAVO dataset with multiple missing traces. The interpolation results are presented in Tab. VI. Comparing the interpolation performance of Algorithm 2 based on DDPM and DDIM, it can be demonstrated that our proposed implicit interpolation significantly enhances the quality of signal recovery with an increase of 0.749 on SNR and PSNR. It is infeasible to explore all potential scenarios for diffusion sampling steps m , jump length L , and jump height H . Therefore, we aim to identify the most feasible options. To select the most suitable hyperparameters, we conduct algorithm 2 repeatedly, applying various combinations. First, based on the trained DDPM, DDIM conducts m -step sampling. While increasing the number of sampling steps enhances the diffusion effect, it poses a higher computational burden during testing. The comparison of the performance of DDPM without the resampling strategy (last three rows in Tab. VI) reveals that a smaller value of m can be selected without significantly sacrificing performance. Consequently, we eventually adopt $m = 100$. Second, in regard to the values of L and H , it is easily found that an increase in their values results in an improved interpolation performance. However, this is accompanied by an increase in testing time. After considering both factors, $L = 10$ and $H = 1$ are ultimately

chosen in our model.

TABLE VI
ABLATION OF VARIOUS SETTINGS OF IMPLICIT INTERPOLATION AND RESAMPLING STRATEGY.

Diffusion model	m	L	H	MSE	SNR	PSNR	SSIM
DDIM	100	10	1	2.123e-04	31.302	36.812	0.957
	100	15	1	2.054e-04	31.469	36.979	0.958
	100	5	1	2.232e-04	31.070	36.580	0.956
DDIM	100	2	1	2.423e-04	30.734	36.244	0.953
	100	1	1	7.498e-04	25.816	31.326	0.903
	100	10	10	2.685e-04	30.301	35.811	0.948
	100	2	2	3.108e-04	29.665	35.175	0.934
DDPM	100	10	1	2.520e-04	30.553	36.063	0.944
	1000	1	1	3.169e-04	29.517	35.027	0.942
	500	1	1	3.288e-04	29.384	34.894	0.940
	100	1	1	4.065e-04	28.496	34.006	0.919

V. CONCLUSION

In this paper, we propose the SeisDDIMR method, which tackles the seismic data interpolation problem with a higher model robustness on various missing data scenarios. SeisDDIMR consists of two processes, including the training of seismic DDPM and implicit conditional interpolation with resampling. Seismic DDPM embeds seismic data into a denoising probability model framework. It achieves full-stage

parameter sharing using the noise matching network based on the U-Net structure equipped with MHSA. The cosine noise schedule is introduced to speed up the transition during the high noise stage of seismic data. Implicit conditional interpolation with resampling, serving as the inference process of seismic DDPM, achieves flexible interpolation for different missing data scenarios and missing rates by utilizing the existing traces of the seismic data as a condition. Interpolation experiments on synthetic and field seismic data with multiple patterns of missing data demonstrate that our SeisDDIMR provides superior quality than existing methods and it also has advantages in robustness. Uncertainty quantification is provided to promote practical applications. In addition, a series of ablation experiments verify the rationality and effectiveness of hyperparameters and the design of key model components. In future studies, we will focus on extending our method to 3D or higher-dimensional seismic data interpolation.

ACKNOWLEDGMENT

The authors would like to thank the Sandia National Laboratory and Mobil Oil Company for providing open data sets.

REFERENCES

- [1] Y. Chen, X. Chen, Y. Wang, and S. Zu, "The interpolation of sparse geophysical data," *Surveys in Geophysics*, vol. 40, no. 1, pp. 73–105, 2019.
- [2] Y. Liu and S. Fomel, "Seismic data interpolation beyond aliasing using regularized nonstationary autoregression," *Geophysics*, vol. 76, no. 5, pp. V69–V77, 2011.
- [3] C. Li, G. Liu, Z. Hao, S. Zu, F. Mi, and X. Chen, "Multidimensional seismic data reconstruction using frequency-domain adaptive prediction-error filter," *IEEE Transactions on Geoscience and Remote Sensing*, vol. 56, no. 4, pp. 2328–2336, 2017.
- [4] Y. Chen, S. Fomel, H. Wang, and S. Zu, "5d dealiased seismic data interpolation using nonstationary prediction-error filter," *Geophysics*, vol. 86, no. 5, pp. V419–V429, 2021.
- [5] S. Fomel, "Seismic reflection data interpolation with differential offset and shot continuation," *Geophysics*, vol. 68, no. 2, pp. 733–744, 2003.
- [6] P. Zwartjes and A. Gisolf, "Fourier reconstruction with sparse inversion," *Geophysical Prospecting*, vol. 55, no. 2, pp. 199–221, 2007.
- [7] F. J. Herrmann and G. Hennenfent, "Non-parametric seismic data recovery with curvelet frames," *Geophysical Journal International*, vol. 173, no. 1, pp. 233–248, 2008.
- [8] S. Gan, S. Wang, Y. Chen, Y. Zhang, and Z. Jin, "Dealiased seismic data interpolation using seislet transform with low-frequency constraint," *IEEE Geoscience and Remote Sensing Letters*, vol. 12, no. 10, pp. 2150–2154, 2015.
- [9] R. Abma and N. Kabir, "3D interpolation of irregular data with a POCS algorithm," *Geophysics*, vol. 71, no. 6, pp. E91–E97, 2006.
- [10] J.-J. Gao, X.-H. Chen, J.-Y. Li, G.-C. Liu, and J. Ma, "Irregular seismic data reconstruction based on exponential threshold model of POCS method," *Applied Geophysics*, vol. 7, pp. 229–238, 2010.
- [11] B. Wang, R.-S. Wu, Y. Geng, and X. Chen, "Dreamlet-based interpolation using POCS method," *Journal of Applied Geophysics*, vol. 109, pp. 256–265, 2014.
- [12] V. Oropeza and M. Sacchi, "Simultaneous seismic data denoising and reconstruction via multichannel singular spectrum analysis," *Geophysics*, vol. 76, no. 3, pp. V25–V32, 2011.
- [13] J. Ma, "Three-dimensional irregular seismic data reconstruction via low-rank matrix completion," *Geophysics*, vol. 78, no. 5, pp. V181–V192, 2013.
- [14] Y. Chen, M. Bai, Z. Guan, Q. Zhang, M. Zhang, and H. Wang, "Five-dimensional seismic data reconstruction using the optimally damped rank-reduction method," *Geophysical Journal International*, vol. 218, no. 1, pp. 224–246, 2019.
- [15] Y. Wang, B. Wang, N. Tu, and J. Geng, "Seismic trace interpolation for irregularly sampled data using convolutional autoencoder," *Geophysics*, vol. 85, no. 2, pp. V119–V130, 2020.
- [16] X. Chai, G. Tang, S. Wang, K. Lin, and R. Peng, "Deep learning for irregularly and regularly missing 3-D data reconstruction," *IEEE Transactions on Geoscience and Remote Sensing*, vol. 59, no. 7, pp. 6244–6265, 2020.
- [17] S. Mandelli, F. Borra, V. Lipari, P. Bestagini, A. Sarti, and S. Tubaro, "Seismic data interpolation through convolutional autoencoder," in *SEG Technical Program Expanded Abstracts*, 2018, pp. 4101–4105.
- [18] W. Fang, L. Fu, M. Zhang, and Z. Li, "Seismic data interpolation based on U-net with texture loss," *Geophysics*, vol. 86, no. 1, pp. V41–V54, 2021.
- [19] B. Wang, N. Zhang, W. Lu, and J. Wang, "Deep-learning-based seismic data interpolation: A preliminary result," *Geophysics*, vol. 84, no. 1, pp. V11–V20, 2019.
- [20] N. Liu, L. Wu, J. Wang, H. Wu, J. Gao, and D. Wang, "Seismic data reconstruction via wavelet-based residual deep learning," *IEEE Transactions on Geoscience and Remote Sensing*, vol. 60, no. 4508213, 2022.
- [21] Y. Lou, L. Wu, L. Liu, K. Yu, N. Liu, Z. Wang, and W. Wang, "Irregularly sampled seismic data interpolation via wavelet-based convolutional block attention deep learning," *Artificial Intelligence in Geosciences*, vol. 3, pp. 192–202, 2022.
- [22] A. Song, C. Wang, C. Zhang, J. Zhang, and D. Xiong, "Seismic data reconstruction via recurrent residual multiscale inference," *IEEE Geoscience and Remote Sensing Letters*, vol. 19, no. 8029105, 2022.
- [23] J. Yu and B. Wu, "Attention and hybrid loss guided deep learning for consecutively missing seismic data reconstruction," *IEEE Transactions on Geoscience and Remote Sensing*, vol. 60, no. 5902108, 2022.
- [24] P. Yuan, S. Wang, W. Hu, P. Nadukandi, G. O. Botero, X. Wu, H. V. Nguyen, and J. Chen, "Self-supervised learning for efficient antialiasing seismic data interpolation," *IEEE Transactions on Geoscience and Remote Sensing*, vol. 60, no. 5913819, 2022.
- [25] A. Song, C. Wang, C. Zhang, J. Zhang, D. Xiong, and X. Wei, "Regeneration-constrained self-supervised seismic data interpolation," *IEEE Transactions on Geoscience and Remote Sensing*, vol. 61, no. 5901610, 2023.
- [26] G. Wu, Y. Liu, C. Liu, Z. Zheng, and Y. Cui, "Seismic data interpolation using deeply supervised U-Net++ with natural seismic training sets," *Geophysical Prospecting*, vol. 71, no. 2, pp. 227–244, 2023.
- [27] S. Pan, K. Chen, J. Chen, Z. Qin, Q. Cui, and J. Li, "A partial convolution-based deep-learning network for seismic data regularization," *Computers & Geosciences*, vol. 145, p. 104609, 2020.
- [28] H. Park, J.-W. Lee, J. Hwang, and D.-J. Min, "Coarse-refine network with upsampling techniques and fourier loss for the reconstruction of missing seismic data," *IEEE Transactions on Geoscience and Remote Sensing*, vol. 60, no. 5917615, 2022.
- [29] T. He, B. Wu, and X. Zhu, "Seismic data consecutively missing trace interpolation based on multistage neural network training process," *IEEE Geoscience and Remote Sensing Letters*, vol. 19, no. 7504105, 2022.
- [30] H. Kaur, N. Pham, and S. Fomel, "Seismic data interpolation using CycleGAN," in *SEG Technical Program Expanded Abstracts*, 2019, pp. 2202–2206.
- [31] D. A. Oliveira, R. S. Ferreira, R. Silva, and E. V. Brazil, "Interpolating seismic data with conditional generative adver-

serial networks,” *IEEE Geoscience and Remote Sensing Letters*, vol. 15, no. 12, pp. 1952–1956, 2018.

- [32] D. Chang, W. Yang, X. Yong, G. Zhang, W. Wang, H. Li, and Y. Wang, “Seismic data interpolation using dual-domain conditional generative adversarial networks,” *IEEE Geoscience and Remote Sensing Letters*, vol. 18, no. 10, pp. 1856–1860, 2020.
- [33] Q. Wei and X. Li, “Big gaps seismic data interpolation using conditional Wasserstein generative adversarial networks with gradient penalty,” *Exploration Geophysics*, vol. 53, no. 5, pp. 477–486, 2022.
- [34] X. Wei, C. Zhang, H. Wang, Z. Zhao, D. Xiong, S. Xu, J. Zhang, and S.-W. Kim, “Hybrid loss-guided coarse-to-fine model for seismic data consecutively missing trace reconstruction,” *IEEE Transactions on Geoscience and Remote Sensing*, vol. 60, no. 5923315, 2022.
- [35] A. Creswell, T. White, V. Dumoulin, K. Arulkumaran, B. Sengupta, and A. A. Bharath, “Generative adversarial networks: An overview,” *IEEE Signal Processing Magazine*, vol. 35, no. 1, pp. 53–65, 2018.
- [36] J. Ho, A. Jain, and P. Abbeel, “Denoising diffusion probabilistic models,” *Advances in Neural Information Processing Systems*, vol. 33, pp. 6840–6851, 2020.
- [37] J. Song, C. Meng, and S. Ermon, “Denoising diffusion implicit models,” in *International Conference on Learning Representations*, 2021.
- [38] A. Lugmayr, M. Danelljan, A. Romero, F. Yu, R. Timofte, and L. Van Gool, “Repaint: Inpainting using denoising diffusion probabilistic models,” in *Proceedings of the IEEE/CVF Conference on Computer Vision and Pattern Recognition*, 2022, pp. 11 461–11 471.
- [39] A. Q. Nichol and P. Dhariwal, “Improved denoising diffusion probabilistic models,” in *International Conference on Machine Learning*, 2021, pp. 8162–8171.
- [40] A. Vaswani, N. Shazeer, N. Parmar, J. Uszkoreit, L. Jones, A. N. Gomez, Ł. Kaiser, and I. Polosukhin, “Attention is all you need,” *Advances in Neural Information Processing Systems*, vol. 30, 2017.
- [41] R. Durall, A. Ghanim, M. Fernandez, N. Ettrich, and J. Keuper, “Deep diffusion models for seismic processing,” *Computers & Geosciences*, p. 105377, 2023.
- [42] P. Dhariwal and A. Nichol, “Diffusion models beat GANs on image synthesis,” *Advances in Neural Information Processing Systems*, vol. 34, pp. 8780–8794, 2021.
- [43] Z. Wang, A. Bovik, H. Sheikh, and E. Simoncelli, “Image quality assessment: from error visibility to structural similarity,” *IEEE Transactions on Image Processing*, vol. 13, no. 4, pp. 600–612, 2004.
- [44] J. Gawlikowski, C. R. N. Tassi, M. Ali, J. Lee, M. Humt, J. Feng, A. Kruspe, R. Triebel, P. Jung, R. Roscher *et al.*, “A survey of uncertainty in deep neural networks,” *arXiv preprint arXiv:2107.03342*, 2021.



Xiaoli Wei is currently pursuing the Ph.D. degree in statistics with the School of Mathematics and Statistics, Xi’an Jiaotong University, Xi’an, China. Her research interests include seismic data reconstruction, deep learning, and uncertainty estimation.



Chunxia Zhang received her Ph.D degree in Applied Mathematics from Xi’an Jiaotong University, Xi’an, China, in 2010. Currently, she is a Professor in School of Mathematics and Statistics at Xi’an Jiaotong University. She has authored and coauthored about 30 journal papers on ensemble learning techniques, nonparametric regression, etc. Her main interests are in the area of ensemble learning, variable selection, and deep learning.



Hongtao Wang is currently pursuing the Ph.D. degree in statistics with the School of Mathematics and Statistics, Xi’an Jiaotong University, Xi’an, China. His research interests include Bayesian statistics and deep learning.



Chengli Tan received the B.S. degree in information and computing science and the M.S. degree in statistics from Xian Jiaotong University, Xian, China, in 2014 and 2017, where he is now pursuing the Ph.D. degree. His current research interests include adversarial learning, Bayesian nonparametrics, and stochastic optimization.



Deng Xiong is a PhD in Geophysics. He currently works for BGP, and serves as a Senior Engineer in R&D Center. He received his PhD from institute of Geology & Geophysics, Chinese Academy of Sciences in 2008. He is interested in near-surface velocity model building and seismic data reconstruction researches in recent years, and presently focuses on some industrial applications of artificial intelligence methods in seismic deblending and regularizations.



Baisong Jiang is currently pursuing the Ph.D. degree in statistics with the School of Mathematics and Statistics, Xi’an Jiaotong University, Xi’an, China. His research interests include seismic data reconstruction, deep learning, and image inpainting.



Jianshe Zhang received the M.S. and Ph.D. degrees in applied mathematics from Xi’an Jiaotong University, Xi’an, China, in 1987 and 1993, respectively, where he is currently a Professor with the Department of Statistics. He has authored and co-authored one monograph and over 80 conference and journal publications on optimization, and remote sensing image processing. His current research interests include Bayesian statistics, global optimization, ensemble learning, and deep learning.



Sang-Woon Kim received the ME and the PhD degrees from Yonsei University, Seoul, Korea in 1980 and 1988, respectively, both in Electronic Engineering. In 1989, he joined the Department of Computer Engineering at Myongji University. Since 2019, he has continued his research as an Emeritus Professor there. His research interests include Statistical Pattern Recognition, Machine Learning. He is the author or coauthor of 51 regular papers and 13 books. He is a Life Senior Member of the IEEE and a member of the IEEK.